Three-component planar velocity measurements using Mach–Zehnder interferometric filter-based planar Doppler velocimetry (MZI-PDV)

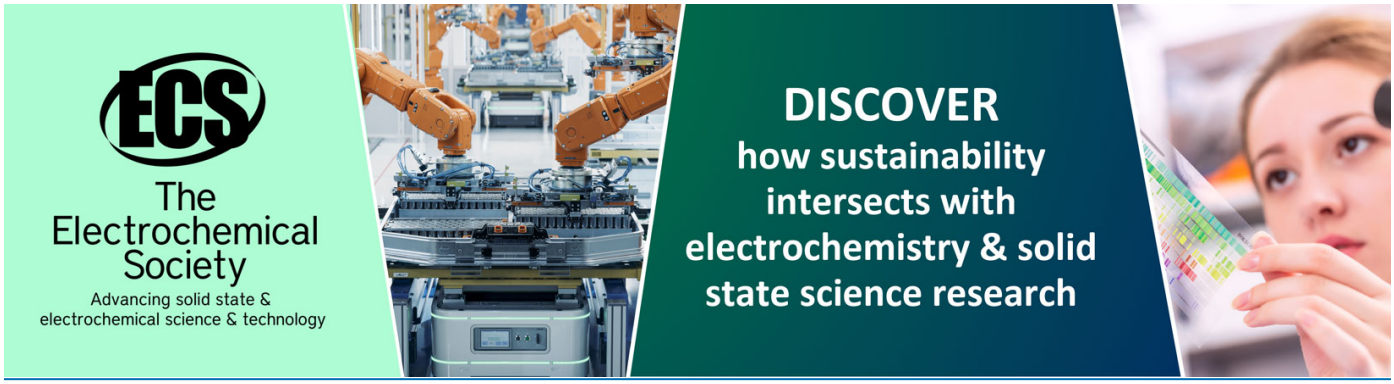

Meas. Sci. Technol. **20** (2009) 034019 (15pp) doi:10.1088/0957-0233/20/3/034019

Three-component planar velocity measurements using Mach–Zehnder interferometric filter-based planar Doppler velocimetry (MZI-PDV)

Z-H Lu, T O H Charrett and R P Tatam

Engineering Photonics Group, School of Engineering, Cranfield University, Cranfield, Bedford MK43 0AL, UK

E-mail: r.p.tatam@cranfield.ac.uk

Received 10 August 2008, in final form 5 January 2009
Published 4 February 2009
Online at stacks.iop.org/MST/20/034019

Abstract
Interferometric filter-based planar Doppler velocimetry is used in conjunction with imaging fibre bundles to make time-averaged three-component velocity measurements using a single imaging head. The Doppler frequency shifts of light scattered by particles entrained into the flow to be measured are transduced to intensity variations using a Mach–Zehnder interferometer. The free spectral range of the filter can be selected by adjusting the optical path difference of the interferometer. This allows the velocity measurement range, sensitivity and resolution to be varied. Three-component measurements are made possible by porting different views of the measurement plane to a single imaging head using the imaging fibre bundles. A comparison of three different image-processing techniques is presented and analysed with the aid of modelled images. Results are presented here for time-averaged measurements of a rotating disc with maximum velocities of $\sim \pm 34$ m s^{-1} in the field of view with the computed measurement error in the orthogonal velocity components being (0.89, 0.68, 1.42) m s^{-1} for the measurement geometry used. Three-component velocity measurements were also made on a seeded air jet with a nozzle diameter of 20 mm and an exit velocity of $\sim$85 m s^{-1}.

Keywords: optical fibre imaging bundles, optical flow measurement, full-field, three-component flow measurement, Fourier processing

(Some figures in this article are in colour only in the electronic version)

1. Introduction

Measurement of fluid flows is of fundamental importance in improving design, reducing emissions and noise in a variety of engineering applications, both in external aerodynamics, e.g. wind tunnel measurements for vehicle prototypes in the aerospace and automotive industries, and in internal flows such as turbo machinery. Point measurement techniques [1] such as laser Doppler and laser transit anemometry (LDA and LTA) are well established and instrumentation is commercially available, but to build up a three-component velocity vector map with good spatial resolution over an extended area requires a large number of individual measurements which can be time consuming and costly. There is, therefore, great interest in techniques that can provide measurements quickly and over large areas.

Planar Doppler velocimetry (PDV) [2, 3], also known as Doppler global velocimetry (DGV) [4, 5], is a relatively recently developed technique that allows the measurement of the velocity over a plane defined by a laser light sheet by measuring the Doppler frequency shift of light scattered from particles in the flow:

$$\Delta\nu = \frac{\nu_0(\hat{o} - \hat{i}) \cdot \bar{V}}{c} \quad (1)$$

where $\Delta\nu$ is the Doppler frequency shift of the scattered light, ν_0 is the illumination frequency and $\bar{V}$ is the velocity vector associated with the scattering particles, c is the free space speed of light and $\hat{o}$ and $\hat{\imath}$ are the unit vectors in the observation and illumination directions, respectively. A single observation and illumination direction allows only a single component of the velocity to be measured; therefore, to make three-component velocity measurements, at least three observation directions and a single illumination direction (or three illumination directions and a single observation direction) are necessary.

In conventional PDV, an atomic or molecular vapour cell, generally containing iodine vapour for operation with lasers in the 500–540 nm region, is used to transduce the Doppler shift in the scattered laser light to an intensity variation [6]. By selecting the illumination frequency to coincide with an absorption line of the gas, the received intensity at the CCD camera is directly related to the Doppler shift, and hence the flow velocity. A reference camera, viewing the flow directly, is usually used to normalize the signal for variations in scattered light intensity due to effects other than the flow velocity. However, the use of molecular gas filters has several disadvantages. The first is that the choice of lasers is limited by the requirement to be able to tune to an appropriate absorption line. The second is that the transfer function is determined by the form of the gas absorption line and therefore the sensitivity cannot be varied greatly, although it is possible to change the shape of the spectral feature by varying the concentration of iodine, the cell temperature or by the addition of buffer gases to broaden the absorption line [6].

Optical interferometry, another technique for frequency-to-intensity conversion, also allows the visualization of a flow field. By using a path length imbalanced interferometer (described in section 2), the Doppler-shifted light scattered from particles entrained in a flow leads to a change of the light intensity distribution in the interference pattern. The magnitude of the change in the fringe pattern is proportional to the flow velocity and the path imbalance in the interferometer. For planar velocity measurements Michelson interferometer configurations have been used previously [7–11]. Michelson interferometers have many advantages for this purpose. They offer large path differences, allowing greater sensitivity, in a compact instrument, which also helps to reduce sensitivity to environmental perturbations such as temperature variations and mechanical vibrations. However, because only one output can be accessed [10], additional optical parts are necessary to obtain a normalized signal to correct for variations in scattered light intensity.

Recently, a Mach–Zehnder interferometer (MZI) based filter has been developed for planar Doppler velocimetry (MZI-PDV) measurements [12]. The use of an MZI as a filter provides two complementary outputs, allowing the scattered light intensity to be normalized by taking the difference of the two outputs divided by the sum. The path length imbalance, necessary to obtain a phase change from the Doppler frequency shift of the scattered light, can be selected to correspond to the expected range of velocities in a given flow situation. A further potential advantage is that any continuous wave or pulsed laser of sufficient power and narrow linewidth can be used as the light source. This paper reports recent developments in the technique; the use of imaging fibre bundles to simultaneously port multiple views of the flow to a single detector head allows three-component planar velocity measurements to be made. Also the data processing scheme is reviewed and an improved method using Fourier domain techniques is reported.

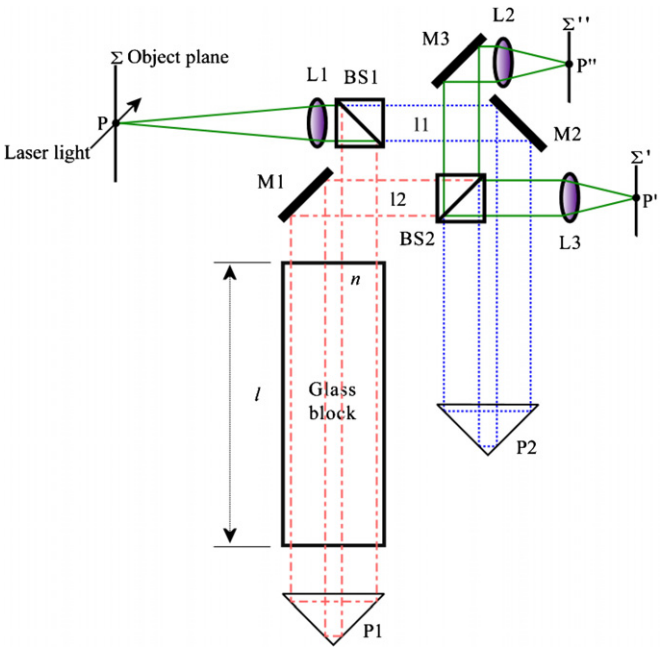

Figure 1. An unbalanced Mach–Zehnder interferometer for PDV. The beam paths are shown in different colours: path l1 in blue (dashed), path l2 in red (dot-dashed) and combined paths in green (solid). (Colour online.)

2. Mach–Zehnder PDV interferometer (MZI-PDV)

In a two-beam interferometer, the phase difference (φ) is a function of the optical path difference (Δl) between the two arms, the light frequency (ν) and the speed of light (c):

$$\varphi = \frac{2\pi\,\Delta l}{c}\nu. \tag{2}$$

Any change in the optical frequency will also cause a change in the phase difference. In PDV, this frequency shift will be caused by the Doppler shift of light scattered from the particles entrained in the flow. The relationship between the Doppler frequency shift ($\Delta\nu$), path length imbalance and the change in the phase difference ($\Delta\varphi$) can be found by differentiating equation (2) with respect to the optical frequency and rewriting in terms of the finite differences:

$$\frac{\delta\varphi}{\delta\nu} = \frac{2\pi\,\Delta l}{c} \quad \rightarrow \quad \frac{\Delta\varphi}{\Delta\nu} = \frac{2\pi\,\Delta l}{c}. \tag{3}$$

Figure 1 shows the arrangement of an unbalanced MZI for PDV. A laser light sheet, of frequency ν_0, illuminates the object plane Σ located in the flow. Light scattered from particles seeded in the flow is collected and coupled into the interferometer. Frequency variations caused by the Doppler shift are converted into variations in the recorded intensities on CCD detectors located at Σ', and Σ''. The scattered light

coming from the object plane Σ is collimated by lens L1 and then divided by BS1 (beam splitter, 50:50 split ratio) into two beams of equal intensity, which follow paths l1 and l2. The light in path l1 is turned at mirror M2 and prism 2 before being split by BS2 and imaged onto the two detectors located at Σ′ and Σ″ using lenses L2 and L3. The second path, l2, passes through a glass block, with a length l and refractive index n. The primary purpose of the glass block is to correct for the difference in magnification and focal distance in the two arms of the interferometer; this is described in more detail by Seiler *et al* [7]. The light is retro-reflected by prism 1, making a second pass through the glass block. It is then turned at mirror M1 and recombined with the light in the first path at BS2.

As the two paths are of unequal optical length, there is a phase difference between the light from each arm, which results in optical interference when the light is recombined and the intensity at the outputs of the interferometer will depend upon the phase difference. For an MZI, the intensity at the two outputs of the interferometer is given by

$$I_1 \propto I_0 \cos^2\left(\frac{\varphi}{2}\right) \tag{4}$$

$$I_2 \propto I_0 \sin^2\left(\frac{\varphi}{2}\right) \tag{5}$$

where I_0 is the scattered light intensity and I_1 and I_2 are the intensities at the two outputs. To normalize the signal, the ratio of the difference over the sums can be used. The normalized intensity, I_N, can be expressed as

$$I_N = \frac{I_1 - I_2}{I_1 + I_2} \propto V\cos(\varphi) \tag{6}$$

where V is the interference fringe visibility determined by the transmission performance of the whole optical set-up. The normalized intensity, I_N, is a function of only the phase difference, φ, between the two arms and is independent of the scattered light intensity, I_0. Therefore, any change in the phase difference will lead to a change in the normalized intensity.

The optical path difference can be varied by changing the length of the glass block (l); this allows the velocity measurement range and resolution to be varied by selecting a suitable path length imbalance and glass block. For example a 5 cm BK7 glass block (refractive index, $n = 1.52$) has a free spectral range (FSR) of about 7 GHz at 514.5 nm; if this is increased to 50 cm, then the FRS is reduced to 0.7 GHz. The technique is therefore limited for low velocities due to the long block length required, which leads to optical distortions, phase instabilities and vignetting effects in the images. These effects are greater for larger optical path differences.

3. Experimental details for a three-component MZI-PDV system

3.1. Imaging fibre bundles

In a conventional PDV arrangement, all three components of the velocity can be obtained by illuminating the flow region of interest from three different directions [13] or collecting the scattering light from three different observation directions [14]. The use of three different illumination directions is unsuitable for instantaneous measurements since each velocity component is measured sequentially rather than simultaneously. The second option requires the use of three imaging heads, each consisting of a pair of cameras (reference and signal) and iodine cell and controller, which can be expensive and complicated. The number of cameras required can be reduced from 6 to 3 by recording the signal and reference images for each observation direction side-by-side on a single camera [15]. This has some drawbacks; the spatial resolution is reduced by a factor of 2 and there is invariably some overlap between the signal and reference images [15]. More recently an optical imaging-fibre-bundle-based PDV technique has been developed by Nobes *et al* [3] at Cranfield University to make instantaneous or time-averaged three-component velocity measurements using only a single imaging head. Willert *et al* [16] and Meyers *et al* [17] have since adopted a similar approach.

In our previous work [12] a 35 mm SLR camera lens was used to image a region of interest in a flow, and this was used as the input to the MZI in the MZI-PDV imaging head arrangement. This allowed only a single velocity component to be measured. Here, the camera lens was replaced with imaging fibre bundles with matched camera lenses at each bundle channel end. This allows multiple velocity components to be measured. The new experimental arrangement is shown in figure 2.

The imaging fibre bundle in use at Cranfield University is a coherent array of fibres that is split into four channels (figure 3(*a*)). Each channel comprises 500 × 600 fibres and is 4 m long. The four channels are joined at the detector head, with each view occupying a quarter of the CCD image shown in figure 3(*b*). The bundle is constructed from 50 μm 'multi-fibre' blocks, shown in figure 3(*c*), of 5 × 5 fibres with 8 μm cores at 10 μm centres [18]. A typical image recorded through the bundles can be seen in figure 4(*a*) and the structure can be seen in the expanded regions in figure 4(*b*). The presence of fringes in these images is discussed further below and the black spots are due to broken fibres. One end of each channel received the image of the flow region using 35 mm SLR camera lenses, although any lens arrangement, including borescopes for internal flows, could be used depending on the flow to be imaged. The transmission through a bundle depends on its length and the operation wavelength. The losses through the bundle are ∼40% for the 4 m length used at a wavelength of 514.5 nm [18].

By using the imaging fibre bundle it is possible to make three-component velocity measurements with only one PDV imaging head arrangement. This reduces the system complexity compared to those reported previously. The use of the fibre imaging bundle also provides more flexibility in viewing arrangements for flows with restricted optical access or unfriendly operating environments such as wind tunnels. This is of particular interest for MZI-PDV as the interferometer can be isolated from the flow environment. Another potential advantage of using the imaging fibre bundle approach is to measure the illumination laser frequency during measurements. This is realised by using the fourth channel to

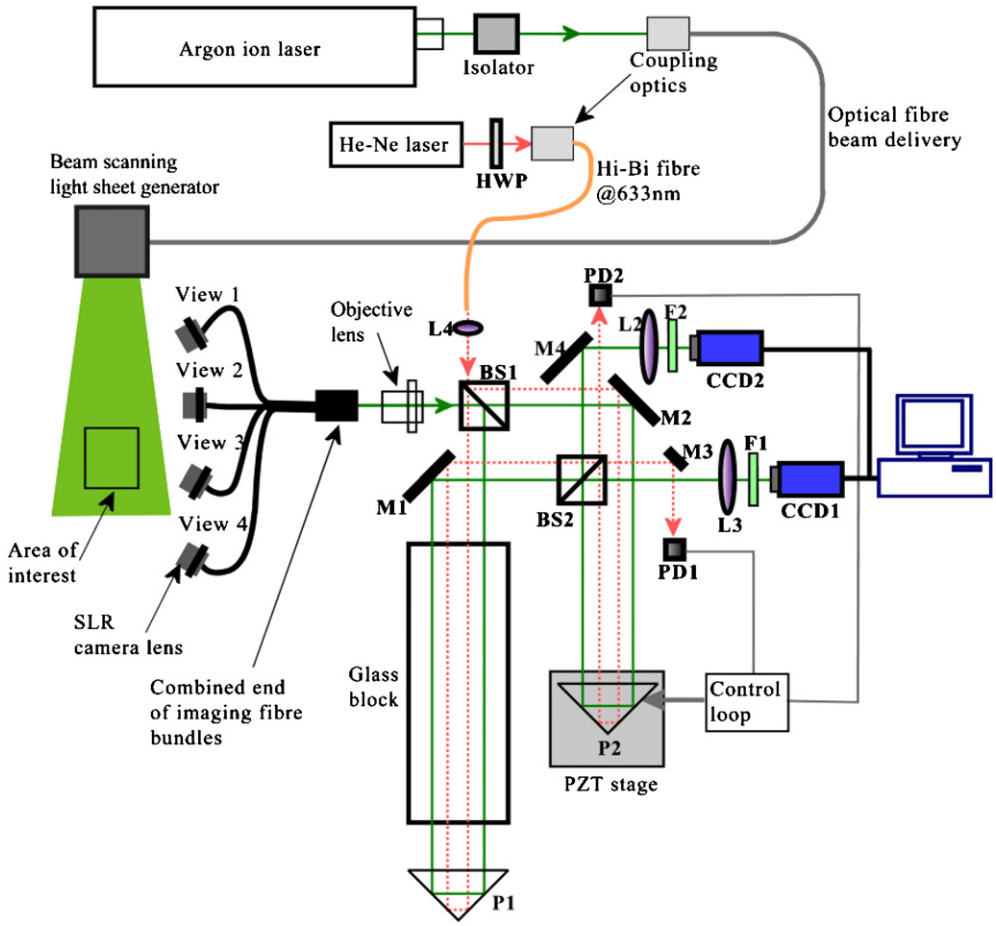

Figure 2. A schematic diagram of the experimental arrangement of the three-component MZI-PDV system using an imaging fibre bundle, including detail of the phase-locking system to stabilize the MZI [10]. HWP: half-wave plate; BS1, 2: 'non-polarizing' beam splitters; L2, 3: tube lenses; L4: coupling lens; M1, 2, 3, 4: mirrors; F1, 2: green filters; P1, 2: right-angle prisms. Beam path for the measurement system shown as solid lines; beam path for phase locking system shown as a dotted line.

monitor the laser frequency in real time by viewing the laser light scattering from a motionless screen. This approach was not used in this work, as the fourth channel was used to measure an additional velocity component to improve the accuracy of the calculation of the orthogonal velocity components [19].

3.2. Illumination system

The illuminating laser was a tuneable continuous-wave argon-ion laser (Spectra Physics Beamlok 2060-7S), incorporating a temperature-stabilized etalon to ensure single-mode operation at 514.5 nm. The stabilized laser, after an ∼30 min warm-up with BeamLok engaged, has a single-mode linewidth of about 3 MHz and an overall residual jitter of ∼10 MHz. The laser frequency drift is about 50 MHz $^{\circ}C^{-1}$. Light from the laser was coupled into an optical fibre through a Faraday isolator, and the output was formed into a light sheet using a prism-scanning device that scanned the beam rapidly across the measurement area. The illumination power after the fibre was ∼200 mW. This arrangement gives an intensity profile of the generated light sheet with an ideal 'top-hat' shape rather than the Gaussian profile formed using cylindrical lenses.

3.3. MZI imaging head arrangement

The scattered light from a flow region was imaged using 35 mm SLR camera lenses and ported to the MZI using the fibre bundle. As in our previous work [12], the MZI was constructed using an infinity-corrected microscope optical system consisting of a matched objective (Plan Apo 1.25x/0.04) and tube lenses ($f = 180$ mm) with a flexible distance between the two called the infinity space. The two complementary output images of the MZI were captured using the two CCD cameras. A photograph of the imaging head arrangement is shown in figure 5 and the dimension is approximately 60 × 90 cm.

The cameras used (LaVision Imager Intense) are scientific grade CCDs operating at −15 °C giving low noise performance. Resolution is 1376 × 1040 pixels with 6.7 × 6.7 μm pixel size, and 12 bit digitization DaVis image processing software was used to control the cameras. The integration time of the cameras is adjustable from 1 ms to 1000 s depending on the scattered light intensity. The camera linearity has been measured previously [20] and is within 1% between 100 and 4000 counts.

Examples of typical images captured at the two outputs are shown in figure 4(*a*). Fringes are formed in the images

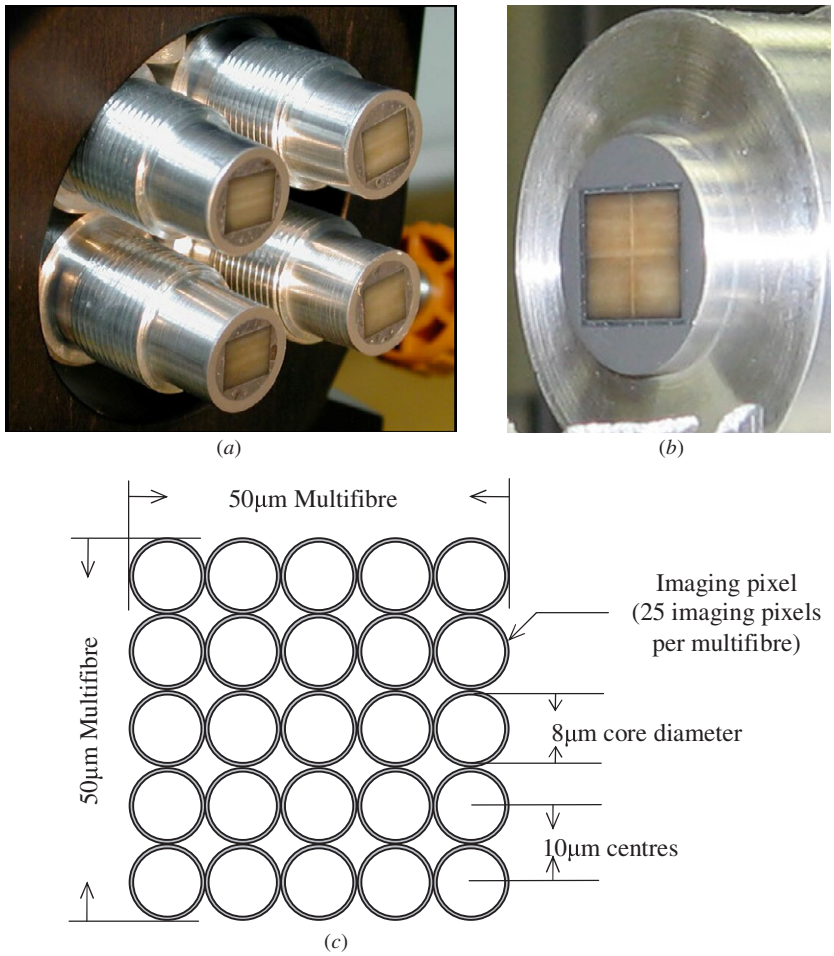

Figure 3. (*a*) Entry faces of the four-channel bundle without imaging lenses. (*b*) Combined exit face of the four channels. (*c*) The structure of one multi-fibre section of the bundle [18].

due to a varying phase difference across the field of view, the resulting fringes are concentric rings centred about the axis of the interferometer. However, due to difficulties in accurately aligning the optical components the fringes will actually appear as curved fringes as show in figure 4, and the number of fringes across the field of view can be adjusted by introducing additional tilt into one arm of the interferometer. The fringes at the two outputs of the interferometer will be in antiphase as can be seen in the magnified region shown in figure 4(*b*).

3.4. Phase stabilization of the interferometer

In order to prevent the interferometer phase drift due to temperature variations and mechanical vibrations, a phase locking system was designed using a feedback loop controller to adjust the path difference of the MZI. This uses a 633 nm beam from a single-frequency stabilized He–Ne laser (Coherent Model: 200), together with green blocking filters, to provide signals for a custom designed PID electronic circuit. More details can be found in [12]. The operational stability depends mainly on the frequency stability of the He–Ne laser (± 2 MHz in 1 hour plus 0.5 MHz $^{\circ}C^{-1}$), corresponding to $\sim \pm 1$ m s^{-1} velocity error. The exact value depends upon the observation and illumination directions. Any frequency drift from this laser will be recorded as an additional constant Doppler shift. Initially a locking signal was generated by picking off a small amount of light from the argon-ion laser. However, stray light, caused by diffraction effects, was found to cause noise on the flow images. As a result, a laser operating at a different wavelength (633 nm) was used with interference filters placed in front of the CCD cameras to block the 633 nm light.

3.5. Image acquisition

To enable three-component velocity measurements, the measured velocity components must first be aligned to a common grid; to enable this the first step is to capture images of a target composed of an array of equally spaced white dots on a black background, aligned in the plane of the laser light sheet. This allows the view of the light sheet to be mapped onto a plane normal to the optical axis. The observation direction, $\hat{o}$, can also be calculated for each pixel in the image using the results of this de-warping process [22] which can then be used to determine the sensitivity vector. In order to calculate the normalized intensity, the two complementary output images (CCD1, CCD2) must be aligned on a pixel-to-

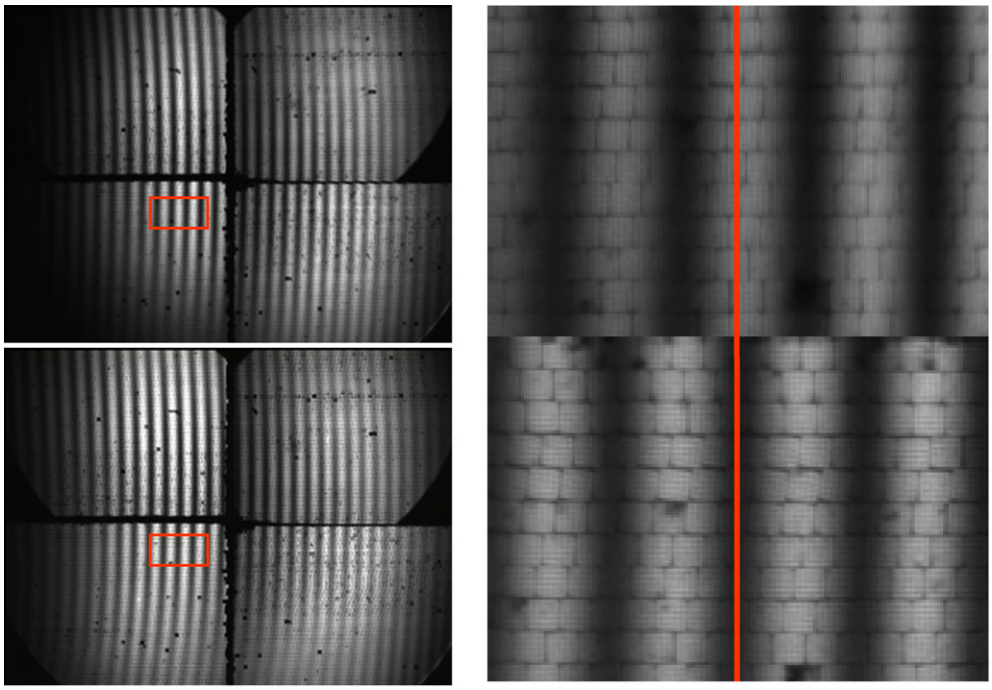

(*a*) (*b*)

Figure 4. (*a*) Example images captured by CCD1 (top) and CCD2 (bottom), showing a rotating disc illuminated with the argon-ion laser at 514.5 nm and viewed using the imaging fibre bundles. (*b*) Magnified section highlighted in (*a*) showing the fringes in antiphase (vertical line) and the fibre bundle structure.

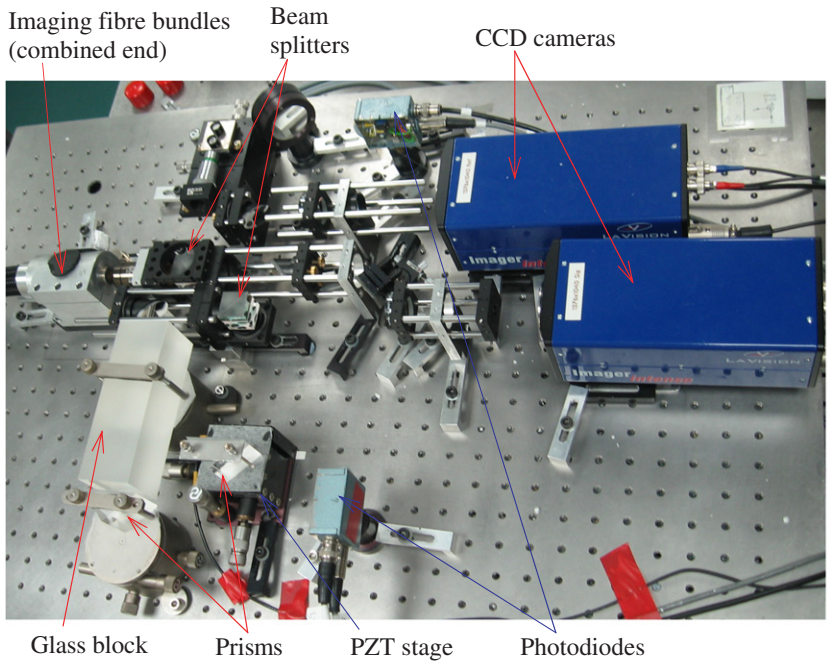

Figure 5. Photograph showing the MZI imaging head arrangement. The dimensions of the imaging head are approximately 60 × 90 cm.

pixel basis to subpixel accuracy. This image mapping process also improves the alignment of the two captured images to each other, removing magnification and distortion variations caused by lens aberrations and imperfections of the beam-splitters, prisms, mirrors and glass block.

Images are then captured under the flow-off and flow-on conditions and the velocity components calculated using the methods described in section 4. The final stage in the processing is to transform from the measured non-orthogonal velocity components to the three orthogonal velocity components, V_X, V_Y and V_Y, aligned with the X, Y and Z axes of the experiment, respectively. At least three different observation directions must be used to measure all three components of the velocity, but the use of the imaging fibre

bundle with four channels provides four measured velocity components. The fourth component can be used to reduce the error introduced in the conversion compared to that using only three measured components [19] either by performing the transformation using all four components or by selecting the three best components.

4. Data processing methods

The key stage in processing is the calculation of the phase shift between the flow-on and flow-off fringe images. Several methods of calculating this phase shift have been investigated; the first uses the shift of the fringe pattern minima and maxima and is described in section 4.1. This method only allows the Doppler shift to be found at positions that correspond with minima in the fringe images, although positions between these can be estimated using interpolation. The other two methods allow a measurement to be made at every pixel. The second method described here and previously reported [12] is the calculation of the phase at every pixel using the normalized intensity and is described in section 4.2. The final method presented here uses Fourier domain processing to evaluate the phase and is described in section 4.3. All the methods described here require images to be captured under zero-velocity conditions and with the flow present to allow the phase shift $\Delta\varphi = (\varphi - \varphi_0)$ to be found. The Doppler shift responsible for a given phase shift can then be found using equation (3):

For a single velocity component measurement system, such as the one described previously in [12], the velocity component can be calculated directly. However, for three-component measurements using imaging fibre bundles some additional steps are necessary. The bundle views are spilt into separate images and de-warped to a common grid. Each velocity component is then calculated using the Doppler equation (1) using the observation and illumination vectors calculated for that view. The final stage is to transform from the non-orthogonal measured velocity components to the orthogonal velocity components aligned with the experimental axis.

4.1. Velocity calculation using fringe skeletonization [8, 12]

The output light intensity of a MZI depends upon its optical phase and the original light intensity distribution, and will have a co-sinusoidal form as given by equations (4) and (5). At $\varphi = \pi, 3\pi, \ldots$ for the first output and $\varphi = 0, 2\pi, \ldots$ for the second output, the intensity will be at a minimum and equidistant minima are present in the recorded images. Similarly maxima will also be present in both images. When the flow velocity causes a Doppler shift in the optical frequency, these fringe patterns will shift; the phase shift can therefore be evaluated at the positions of minima and maxima in the recorded images using

$$\Delta\varphi = 2\pi \frac{\Delta s}{s} \tag{7}$$

where s is the unshifted fringe spacing, Δs is the shift in the fringe position and $\Delta\varphi = (\varphi - \varphi_0)$ is the phase shift. The Doppler shift can then be found using equation (3).

4.2. Phase calculation using the normalized intensity [12]

The second method evaluates the phase difference at each pixel for both the zero-velocity (flow-off) and flow-on images using the normalized intensity; the phase shift can then be found for each pixel. In practice, the range of the normalized intensity will not be within $-1 \leqslant I_N \leqslant 1$ across the whole image due to optical distortions in the MZI. To take account of this, equation (6) can be rewritten as

$$\begin{aligned} I_N(i,j) &= \frac{I_1(i,j) - I_2(i,j)}{I_1(i,j) + I_2(i,j)} \\ &= \left(\frac{I_{N\max}(i,j) + I_{N\min}(i,j)}{2}\right) \\ &\quad + \left(\frac{I_{N\max}(i,j) - I_{N\min}(i,j)}{2}\right)\cos(\varphi(i,j)) \end{aligned} \tag{8}$$

where the indices (i, j) give the pixel position in the images. $I_{N\max}$ and $I_{N\min}$ are the maximum and minimum values for the normalized intensity at each pixel, which can be approximately evaluated from the closest maximum and minimum in the fringe pattern. The phase difference, $\varphi(i, j)$, for each pixel, can then be found by rearranging equation (8):

$$\begin{aligned} \varphi(i,j) &= \arccos\left(\frac{2\cdot I_N(i,j) - (I_{N\max}(i,j) + I_{N\min}(i,j))}{I_{N\max}(i,j) - I_{N\min}(i,j)}\right) \\ &\quad \pm n\pi \qquad n = 0, 1, 2, 3\ldots. \end{aligned} \tag{9}$$

This calculation is performed for both the flow-on and flow-off fringe patterns and the phase shift, $\Delta\varphi$, calculated; the Doppler shift is then calculated using equation (3).

4.3. Phase calculation using Fourier domain processing

A spatial carrier fringe method can be used to evaluate the phase of the recorded fringe patterns [23]. Figure 6 shows an overview of this method for a simulated fringe pattern. Two fringe images are recorded, a flow-off image containing only the carrier fringe phase variation and a flow-on image containing the carrier fringes and an additional phase shift due to the Doppler shift (figure 6(*a*)). The two-dimensional Fourier transformation is calculated for both the flow-on and flow-off fringe images (figure 6(*b*)). One of the side peaks in each of the transformed images is selected and isolated. The inverse two-dimensional FFT and the phase are then calculated using equation (10). This is shown in figure 6(*c*) for both the flow-on and flow-off images:

$$\varphi = \arctan\left(\frac{\mathrm{Im}(c(i,j))}{\mathrm{Re}(c(i,j))}\right). \tag{10}$$

The phase shift can then be calculated by subtracting the flow-on and the flow-off phases (figure 6(*d*)); finally, the Doppler shift can be calculated using equation (3) (figure 6(*e*)).

4.4. Assessment of processing schemes using simulated data

To assess the relative advantages and disadvantages of different processing schemes, a simple computational model was used to simulate MZI fringes from equations (2) to (6). No attempt was made to use the model to predict the error level for an experimental system, as this would require a quantitative

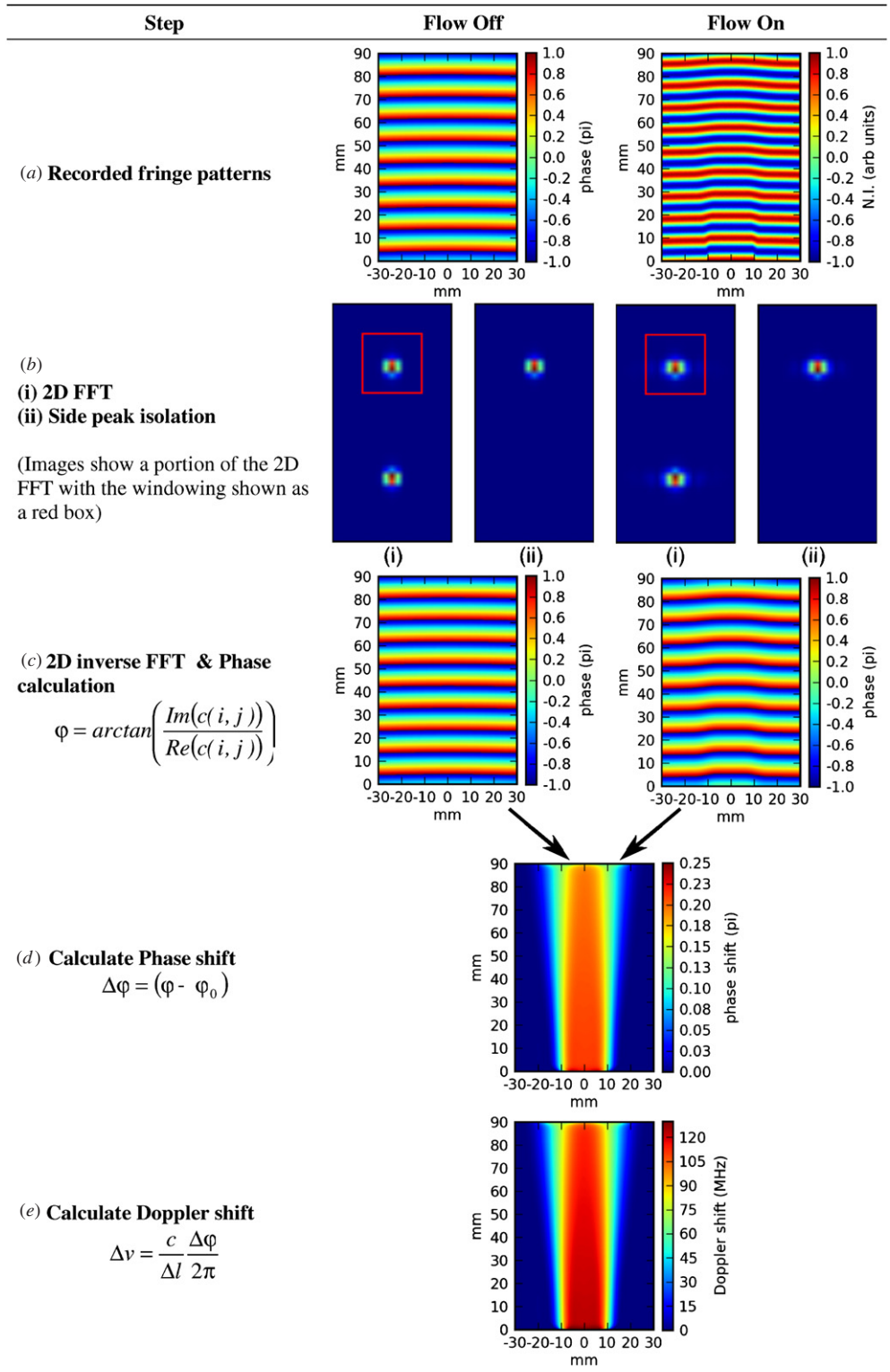

Figure 6. The two-dimensional phase demodulation scheme using simulated data. (*a*) Flow-on and flow-off fringe images are recorded. (*b*) The 2D-FFT of the fringe patterns is calculated. (*c*)–(*d*) The phase from each is calculated independently from the isolated side spectrum. (*e*) The phase shift found by subtraction; the Doppler shift can then be found from this phase shift.

knowledge of the noise sources; rather a representative level of noise was added, similar to that used in previous assessments of uncertainty [19]. Unshifted and shifted fringe images where generated using the theoretical velocity field of an axis symmetric air jet for a single observation direction. Noise was added to these images to simulate CCD noise sources. This noise included typical image noise sources such as photon shot noise, CCD dark-current and the effect of analogue-to-digital truncation, and the levels used were estimated from typical experimental images of ∼2000 counts. The simulated

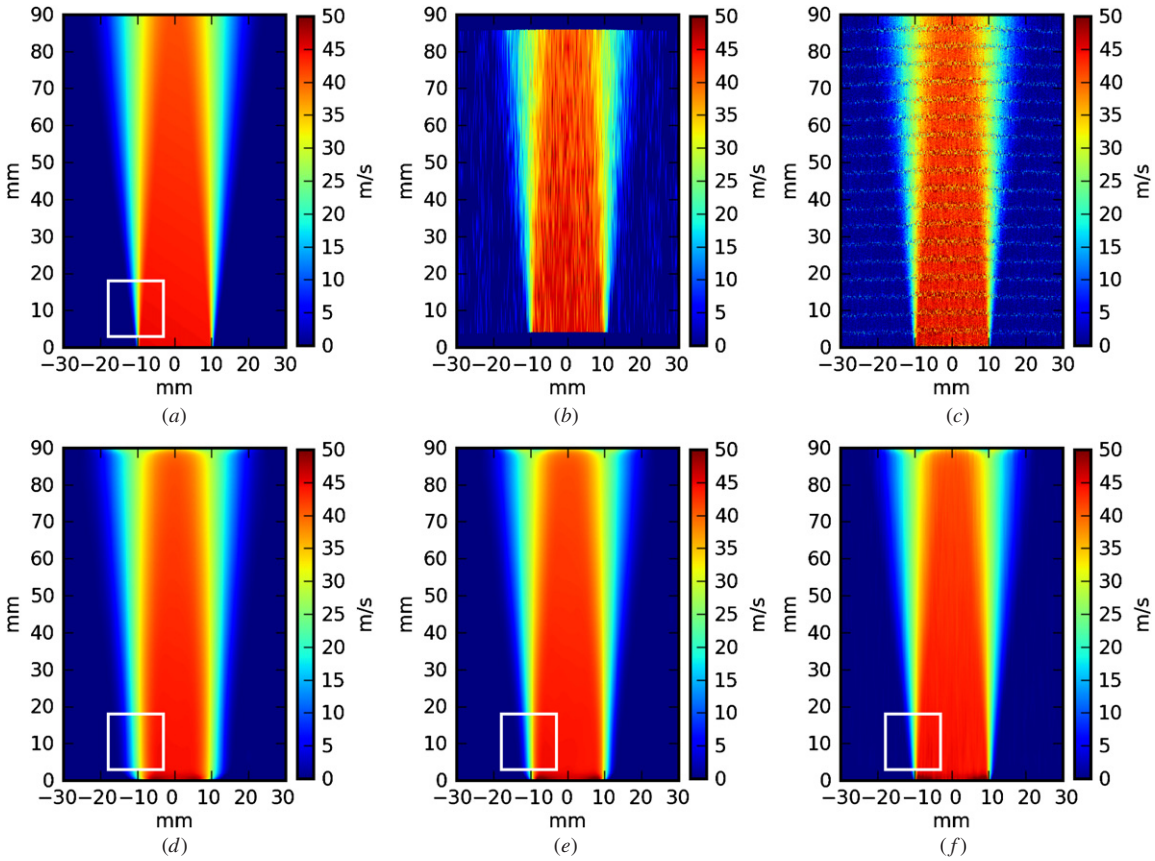

Figure 7. (*a*) The modelled velocity component and the calculated velocity component using (*b*) the fringe skeletonization method and linear interpolation, (*c*) the normalized intensity method and (*d*)–(*f*) the FFT method with increasing window size in the horizontal direction showing the effect of spatial filtering (highlighted in boxes); window sizes: (*d*) 20 pixels-–5% of the image width, (*e*) 40 pixels-–10% of the image width and (*f*) 400 pixels—the full image width.

images were then processed using the three methods described in sections 4.1–4.3. Figure 7(*a*) shows the theoretical velocity component for the observation direction used and figures 7(*b*)–(*f*) show the results of processing the simulated fringe images using different techniques.

The results of the fringe skeletonization method are shown in part (figure 7(*b*)); although this processing technique can only calculate the velocity along fringe minima or maxima, and not across the whole image plane, interpolation of the values between these positions can be used. This causes the vertical streaking seen in figure 7(*b*). Seiler *et al* [8–10] have reported a similar system using a Michelson interferometer. Multiple components of the velocity can be measured using this approach; however, the calculation of orthogonal velocity components is only possible when using interpolation. This is because each velocity component is only calculated at fringe minima/maxima positions and these are unlikely to coincide when multiple components are mapped together. The choice of fringe spacing is important when implementing this method with the calculated velocity being quantized due to the shift and fringe spacing being evaluated to the nearest pixel. The Doppler shift resolution is given by

$$\Delta(\Delta\nu) = \frac{\Delta s}{s}\frac{c}{\Delta l}. \tag{11}$$

However, although fewer fringes will give a better resolution in the Doppler shift, and hence velocity, this will be at the expense of fewer measurement points. This could be avoided if the fringe locations were identified using sub-pixel interpolation. This method also has the advantage that only a single output of the interferometer is necessary and could therefore be applied using only a single CCD camera.

Table 1. Phase shift calculation for the different regions defined in figure 8.

Region	Phase shift calculation
1	$\varphi - \varphi_0$
2	Positive phase shift: $(\varphi + \varphi_0)$ Negative phase shift: $(\varphi + \varphi_0) - 2\pi$
3	$\varphi_0 - \varphi$
4	Positive phase shift: $2\pi - (\varphi + \varphi_0)$ Negative phase shift: $-(\varphi + \varphi_0)$

The results of using the normalized intensity method are shown in figure 7(*c*). This method is sensitive to noise in the fringe patterns especially around the locations of fringe minima and maxima.

The calculation flow-off and flow-on phase vary between zero and π in a sawtooth form as shown in figure 8; therefore the phase shift is required to be calculated differently depending upon the regions defined in table 1. In regions 1 and 3, the phase can be found by subtraction. For regions 2 and 4, the calculation of the phase shift will depend upon the direction

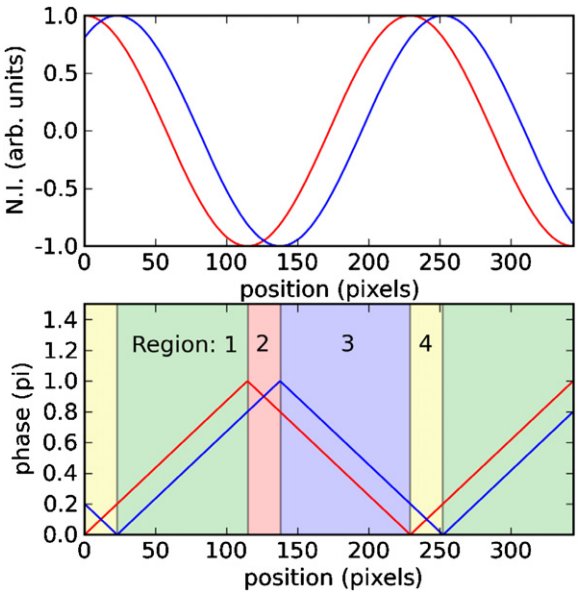

Figure 8. Typical normalized intensity signal (top) for unshifted fringes (red) and shifted fringes (blue) and the calculated phase using the normalized intensity method for each signal. The regions used for the calculation of the phase shift are shaded and labelled with the method used given in table 1. (Colour online.)

of the shift, which is not known. However, as it can be assumed that the phase shift will be within the range $-\pi \leqslant \Delta\varphi \leqslant +\pi$ the correct phase shift can be determined for these regions. The noise present in the data can lead to the region being misidentified around minima and maxima, although this effect could potentially be removed in processing. Also at positions close to maxima and minima, the velocity sensitivity is lower than at the quadrature positions; these effects lead to the striping effect seen in figure 7(*c*).

Figures 7(*d*)–(*f*) show the calculated velocity components using the Fourier domain processing technique described in section 4.3, using various window sizes in the horizontal direction. The window size in the vertical direction cannot be varied greatly due to the need to isolate only one frequency peak (see figure 6(*b*)); here a vertical window dimension of 20 pixels was used. By removing the other frequency components, the carrier fringe pattern is isolated; however this also results in spatial filtering after the inverse transformation. In figure 7(*d*), which shows a window size with a width of 5% of the Fourier domain image (20 pixels), this filtering can be seen in the highlighted rectangle, where the transition from the core (red) to the zero flow region (dark blue) is broader than that for the theoretical velocity shown in (a) (colour online). It is possible to reduce the filtering in the direction parallel to the fringes whilst still isolating the carrier fringe frequency by increasing the window size in this direction. Figures 7(*e*) and (*f*) show the same fringe patterns processed using a window with (*e*) twice the width (40 pixels) and (*f*) the entire image width (400 pixels). The effect of increasing the window size reduces the spatial filtering in this direction. Therefore for this method of processing, care must be taken to ensure that the fringe orientation is considered for the experiment; for example for the jet flow simulated here, a vertical fringe orientation would not be suitable as the carrier frequency could not be isolated without excessive spatial filtering.

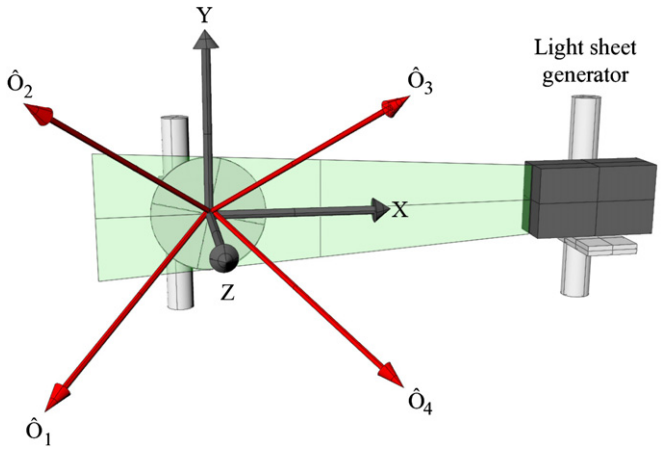

Figure 9. Diagram showing the viewing geometry used when making measurements on the rotating disc. $\hat{o}_1$, $\hat{o}_2$, $\hat{o}_3$ and $\hat{o}_4$ are the observation directions for each arm of the imaging fibre bundle.

5. Results

5.1. Validation measurements on a rotating disc

A rotating disc was used as the first target to validate the three-component MZI-PDV system providing a well-defined velocity field with which to assess the uncertainty. This was also used in the single velocity component MZI-PDV system. The rotating disc is 200 mm in diameter and coated with white paint in order to enhance the light scattering. Figure 9 shows the viewing configuration used to make measurements on the rotating disc, along with the light sheet generator. The surface of the disc defines the *XY* plane and the light sheet was propagating in the negative *X* direction. The four camera lenses were located in the same plane on the positive *Z* side of the light sheet, since only one side of the disc was illuminated. This arrangement gave relatively large Doppler sensitivity vectors, but led to unbalanced intensities collected in the four views because $\hat{o}_3$ and $\hat{o}_4$ were in the forward scattering direction while $\hat{o}_1$ and $\hat{o}_2$ were in the backward scattering direction. The four arms of the imaging fibre bundle were mounted onto a structure built with FlexLink structural components. This provides a stable structure to mount the imaging lenses so that they are not affected by vibrations related to the running disc or flow. This also provides flexibility in mounting the views so as to obtain a well-conditioned matrix for the transformation used to calculate the orthogonal velocity components [19].

A pair of images were captured simultaneously (one on each CCD camera) with the disc being motionless. The disc rotation was started and a second image pair captured. Example images are shown in figure 4, with the four views having a common field-of-view which covered the central portion of the disc with a diameter of approximately 100 mm. The rotation of the disc was measured independently using an optical tachometer to be 108 Hz giving a maximum

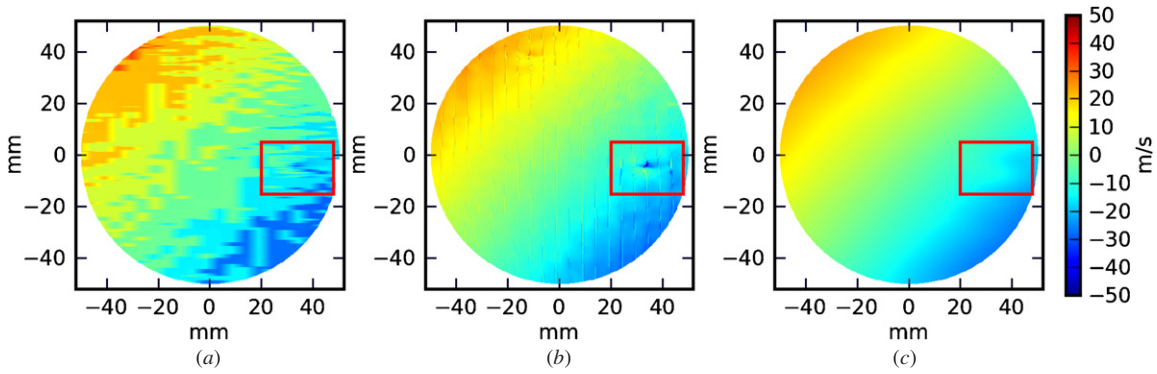

Figure 10. Example of the velocity field of a rotating disc, calculated from view 2 using the different processing techniques described in section 3. Calculated using (*a*) the fringe skeletonization method with the data interpolated between fringe positions, (*b*) the normalized intensity method and (*c*) the Fourier transformation method. The highlighted box indicates the distortion associated with a broken fibre.

Table 2. Comparison between the processing methods used to calculate the velocity component of a rotating disc shown in figure 10.

	Skeletonization	Normalized intensity	FFT
Standard deviation of error	4.45 m s^{-1}	1.96 m s^{-1}	0.83 m s^{-1}
Data points	7146 (before interpolation)	155 892	155 892

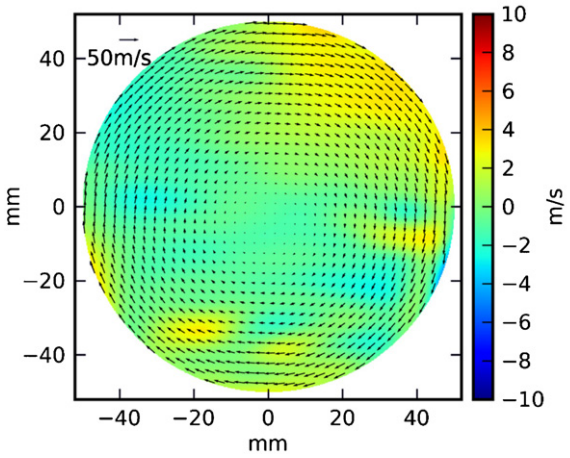

Figure 11. Computed velocity field (4C method) for the rotating disc test object. Vectors show the in-plane velocities (every 12th vector in both the horizontal and vertical directions is shown) and colour shows the out-of-plane velocity. (Colour online.)

circumferential velocity in the common field of view of $\sim\pm34$ m s^{-1}. The fluctuation in the disc's rotation was approximately ±0.1 Hz during the measurement period; this results in an error of $<0.1\%$ which is more than one order of magnitude smaller than other error sources. The images with the disc being stationary exhibit a speckled appearance due to the highly coherent source used, as in the single component measurement reported in [12]. Also some black spots are clearly visible; these are due to broken fibres in the imaging fibre bundle. The invisible or poor-visibility edges of the images are due to the 'vignetting effect' in the imaging system [12]. The optical power at the output of the optical fibre was $\sim$200 mW and the CCD camera integration time was set to be 5 s to obtain clear images. These images were then processed using the methods described above.

Examples of the velocity field calculated from view 2 are shown in figure 10 with a comparison between these methods given in table 2. Figure 10(*a*) was calculated using the fringe skeletonization method, as this method only provides measurement points along fringe positions; points between these were calculated using linear interpolation. This method also requires that the fringe images are filtered to improve the identification of maxima and minima positions; here five runs of a 9 × 9 smoothing filter were used. Figure 10(*b*) was calculated using the normalized intensity method; the calculated result can be seen to be noisy, particularly around fringe positions as anticipated in section 4.4. This can be improved by increasing filtering used before processing, although this is at the expense of spatial resolution. As before, five passes of a 9 × 9 smoothing filter were used. Figure 10(*c*) shows the velocity component calculated using the Fourier transformation method. No additional smoothing was used when processing the data with this method. This method performs significantly better than the others particularly when processing noisier data with the standard deviation of the error (theoretical component minus measured component) being smaller than 1 m s^{-1} for all views. This is a significant improvement over our previous results [12]. A slight distortion from the expected smooth variation can be seen in the highlighted box. This is due to a broken fibre at this location in the image and can also be seen in (*a*) and (*b*). Potentially, the influence of such broken fibres could be reduced by implementing a pre-processing scheme which interpolates the pixel intensities from surrounding pixels to lessen this effect.

The four measured velocity components for the four observation directions are then converted to the orthogonal velocity components V_X, V_Y and V_Z (the horizontal, vertical and out-of-plane components respectively). The computed orthogonal velocity field calculated using FFT methods is shown in figure 11, with the in-plane components shown as vectors and the out-of-plane by the colour scale. This calculation can be done using either three (3C) or all four components (4C), and in previous work at Cranfield

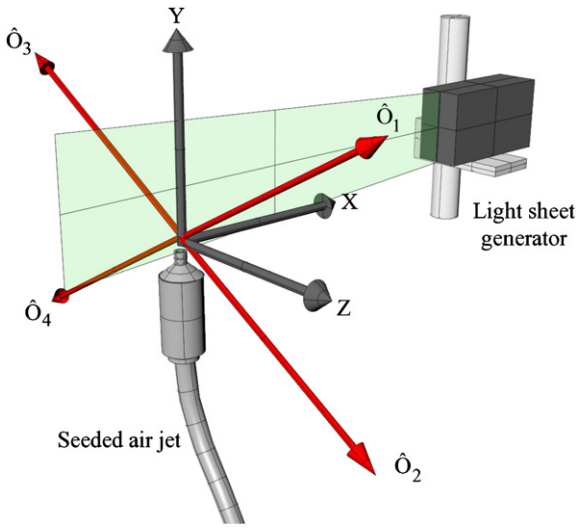

Figure 12. Diagram showing the viewing geometry used when making measurements on an axis-symmetric air jet. $\hat{o}_1$, $\hat{o}_2$, $\hat{o}_3$ and $\hat{o}_4$ are the observation directions for each arm of the imaging fibre bundle.

it has been shown that the use of additional components in this transformation can lead to significant reductions in the error [19]. The standard deviation in the error for the three orthogonal components calculated using three and four components is given in table 3. It can be seen that the use of four components in this calculation does indeed make a significant difference; this effect is greater for disc measurements as all views must be located on one side of the measurement plane and these viewing configurations are not as good as typical flow configurations where views may be located on either side of the light sheet.

Table 3. Standard deviations of the variations between the calculated and theoretical orthogonal velocity components (along the *X*, *Y* and *Z* axes, in figure 9) for the rotating disc.

Standard deviations	V_X	V_Y	V_Z
3C method	1.85 m s^{-1}	0.88 m s^{-1}	1.93 m s^{-1}
4C method	0.89 m s^{-1}	0.68 m s^{-1}	1.42 m s^{-1}
Percentage difference between methods	51%	23%	26%

5.2. Three-component planar velocity measurements on a seeded air jet

The system was then used to make measurements on a velocity field which is more representative of the intended application. For this a seeded air jet, with a 20 mm diameter smooth contraction nozzle, was used to provide a test flow. The exit velocity of the jet was ∼85 m s^{-1}, which was calculated by measuring the nozzle pressure ratio. The air intake to the jet and the surrounding co-flow were seeded using a Concept Engineering Vicount compact smoke generator operating at 37 °C with nitrogen as the propellant gas, which generates smoke particles in the 0.2–0.3 μm diameter range. The observation directions were selected to be in the strong forward scattering so as to ensure sufficient signal on the CCD cameras.

A symmetric viewing arrangement was used to make measurements on this air jet (figure 12). The jet was positioned by using a stable support trestle with the main flow direction in the positive *Y* direction. The laser light sheet penetrated vertically through the flow field in the *X*–*Y* plane. The four imaging camera lenses at the arm ends of the fibre bundles were located symmetrically along the laser sheet in the *Y*–*Z* plane. This arrangement was chosen to optimize the viewing geometry and balance the collected light intensities. In

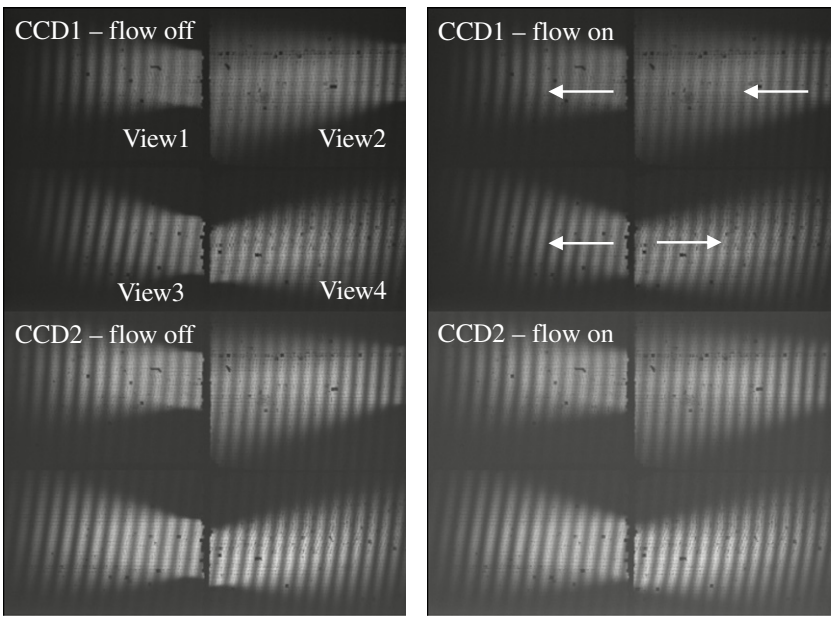

(*a*) (*b*)

Figure 13. Two pairs of fringe images recorded by CCD1 (top) and CCD2 (bottom): for the jet flow-off (*a*) and on (*b*) in the three-component MZI-PDV system. The four views of the flow are labelled in (*a*) and the main flow direction is shown by the arrows in (*b*).

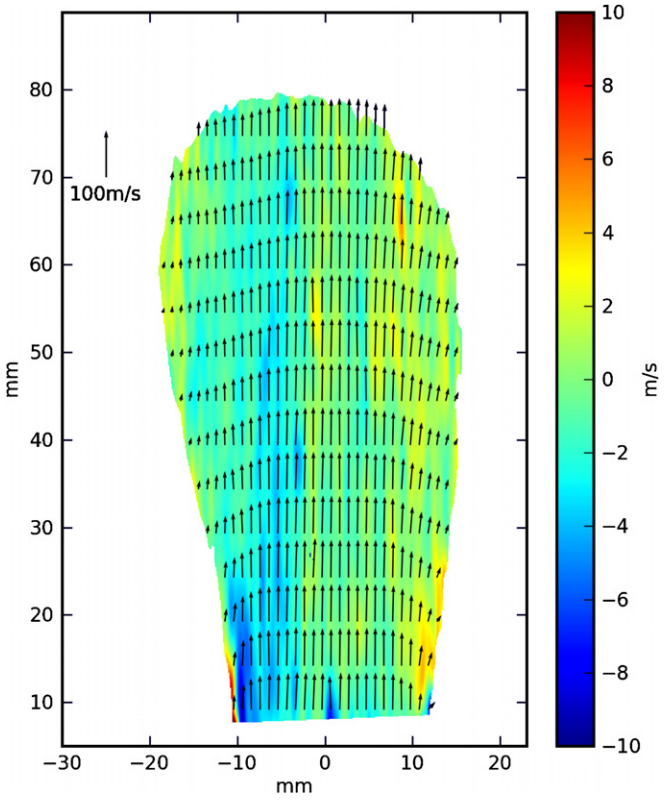

Figure 14. Three-component velocity measurement of an axis-symmetric air jet made using the MZI-PDV system and processed using the FFT method. Vectors show the in-plane velocities (every 10th and 50th vector shown in the horizontal and vertical directions, respectively) and colour the out-of-plane velocity. (Colour online.)

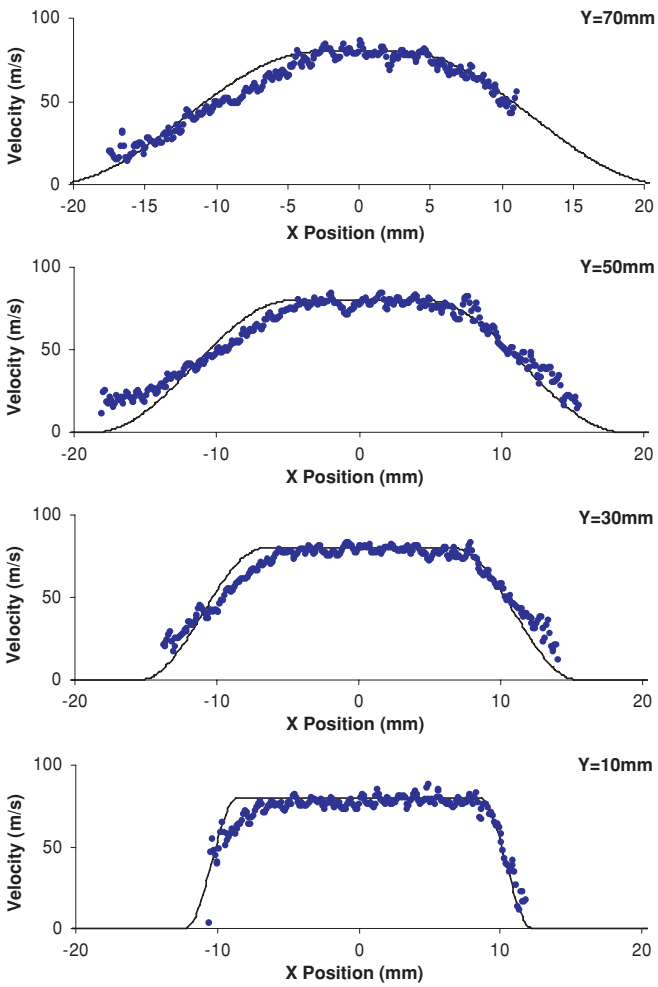

Figure 15. A comparison between profiles taken through the centre of the vertical (V_Y) component of the jet at axial positions $Y = 10$, 30, 50 and 70 mm downstream from the nozzle. Three-component MZI-PDV measurements are shown as blue points, theoretical values are shown as a black line. (Colour online.)

particular, locating views on both sides of the light sheet can lead to significant improvements in the error propagation in the transformation to the orthogonal velocity components [19].

When making single velocity component measurements on the same seeded air jet in our previous work [12], a smooth plate was positioned in the field of view and illuminated by the laser sheet to provide the 'flow-off' phase measurement. However, this was not possible when making three-component measurements since both sides of the light sheet were viewed. Instead, the seeded air jet flow was used to obtain the reference image (zero-velocity phase image) with the jet flow as slow as possible (<1 m s^{-1}). This initial seeded flow field is still termed the 'flow-off' field for convenience in the following text. The advantage of this method is that the plane defined by the laser sheet is exactly the same for the reference image and the flow field image. However, a relative measurement error will be introduced due to the non-zero flow velocity used when the reference image was captured; this was estimated to be smaller than 1 m s^{-1}.

The two pairs of images (flow-off and flow-on) were captured and are shown in figure 13. The four bundle views are labelled and the main flow direction of the jet is shown using the arrows. It should also be noted that the flow direction was actually vertical; however, the imaging fibre bundles have been rotated to maximize the axial measurement area. The measured area was approximately 50 × 90 mm and a camera exposure time of 10 s was used to obtain clear images. These images were then processed to obtain the non-orthogonal velocity components for the four observation directions. These are then converted to the orthogonal velocity components V_X, V_Y and V_Z, the horizontal, vertical and out-of-plane components, respectively, using either three or all four of the measured components.

Figure 14 shows an example of a measured velocity vector map computed using the 4C method for the field of view made on the air jet flow. Vectors indicate the magnitude and the direction of the in-plane components of velocity while the colour map indicates the magnitude of the out-of-plane velocity component. Only every 40th column and every 8th point on each row are shown in this figure. The 'top-hat' velocity profile close to the nozzle exit is what would typically be expected in the near field of the jet. Some regions of the image have poor fringe visibility and a low signal level, due to the vignetting effect described above. Others, for example the outer regions of the jet, have a low signal level due to a lack of seed particles in the flow. Those regions where a reliable

calculation of the velocity field is not possible are masked in the data processing.

A comparison between the profiles of the vertical (V_Y) velocity component taken horizontally through figure 14 is shown in figure 15. Here profiles from axial positions downstream ($Y = 10$, 30, 50 and 70 mm) from the nozzle are shown, along with theoretical values calculated using the empirical equations described by Rajaratnam [24] for a simple axis-symmetric jet flow. In these plots, measurements made using the three-component MZI-PDV are shown as blue points and the theoretical profiles are shown as a solid black line (colour online). It can be seen that there is good agreement between them, in terms of the overall profile of the flow. The measurements towards the outside of the jet flow vary more from the expected values possibly due to less fringe visibility in these regions, lower signal levels resulting from the 'vignetting effect' in the infinity-corrected optical system and lower seeding levels in these regions as well. These results are similar to those obtained using iodine-cell-based PDV measurements for the same air jet [20, 21].

6. Discussion and conclusions

A PDV technique has been described that is capable of measuring the three components of the velocity over a two-dimensional region defined by a laser light sheet, using a Mach–Zehnder interferometric filter. As an extension of previous work at Cranfield [12], in which single velocity component measurements were made, the system was modified to allow all three components of the velocity to be measured using an imaging fibre bundle with four separate channels, combined at one end and separate at the other. Matched camera lenses were used at each channel end to image the field of view, and the output of the combined end of the bundles was used as the input to the MZI. This allows three-component velocity measurements using only a singe imaging head.

Several methods of processing the captured data have been developed with the Fourier-transformation-based processing identified as the most successful, although this technique requires careful selection of the windowing used to avoid excessive spatial filtering. This will be a particular problem when steep velocity gradients are anticipated in the flow field to be measured, with the edge of any such features potentially being blurred.

The rotating disc used in validating the single component MZI-PDV system [12] was again used to validate the three-component system. The use of the FFT processing technique has allowed a significant improvement in the single velocity component measurement error from our previous work [12], with the standard deviation of the error being typically <1 m s^{-1} compared with 1.96 m s^{-1} for the normalized intensity approach used previously. The calculated orthogonal velocity components agree well with those calculated from the optical tachometer measurement. The standard deviations of the velocity error when the calculation is performed using three of the four available components are (1.85, 0.88, 1.93) m s^{-1} for the V_X, V_Y and V_Z components, respectively. The use of redundant data in this calculation, by using the fourth velocity component, results in improvements of (51%, 23%, 26%) in these errors over using three components only, giving velocity errors of (0.89, 0.68, 1.42) m s^{-1} for V_X, V_Y and V_Z.

The system has also been demonstrated by making three-component velocity measurements on a seeded air jet with a maximum exit velocity of $\sim$85 m s^{-1}. The computed velocity field is typical of what can be expected in the near field of the jet and is similar to measurements made previously using Iodine-cell-based PDV techniques, on the same jet [20, 21].

In the current MZI-PDV system, two cameras in the interference fringe planes are required to record both outputs of the MZI, which are similar to signal and reference cameras in a conventional PDV system imaging head. It is also possible to obtain the two complementary outputs using a single camera and the MZI-PDV system by acquiring two sequential frames with a π phase change applied to one arm of the interferometer between successive frames. This technique can be termed single camera MZI-PDV and is similar in concept to 2ν-PDV [20, 21] in which two frames are captured sequentially with a frequency shift applied to the illumination light between frames. The phase change can be readily achieved by adding a constant voltage, synchronized to the camera timing, to the error signal already being used to control the path imbalance for phase locking and control.

As with the 2ν-PDV technique [21], single camera MZI-PDV will have the advantage of avoiding errors introduced by image misalignment since both images are now captured on the same camera. It also reduces complexity and leads to better cost efficiency. However, this technique will be restricted to steady-state flow situations where seeding/scattering needs to be constant because the two images are not taken simultaneously. Another possible problem is the interferometer drift during image acquisition. The technique is currently being investigated and will be reported in the near future.

With the continuous-wave argon-ion laser, the MZI-PDV only can capture time-averaged measurements. In a fast-varying flow, a pulsed laser would be required to make instantaneous measurements. This is currently under investigation.

Acknowledgments

The authors would like to acknowledge H D Ford, for helpful advice and assistance. Zenghai Lu acknowledges an Overseas Research Scholarship (ORS) award from the Committee of Vice Chancellors and Principals, UK. This work was supported by a Paul Instrument Fund grant from the Royal Society, UK, and the Engineering and Physical Sciences Research Council (EPSRC), UK.

References

[1] Tropea C, Yarin A L and Foss J (ed) 2007 *Springer Handbook of Experimental Fluid Mechanics* (Berlin: Springer)
[2] Elliott G S and Beutner T J 1999 Molecular filter based planar Doppler velocimetry *Prog. Aerosp. Sci.* **35** 799–845

[3] Nobes D S, Ford H D and Tatam R P 2004 Instantaneous, three component planar Doppler velocimetry using imaging fibre bundles *Exp. Fluids* **36** 3–10
[4] Meyers J F and Komine H 1991 Doppler global velocimetry: a new way to look at velocity *Laser Anemometry* **1** 273–7
[5] Reinath M S 1997 Doppler global velocimeter development for the large wind tunnels at Ames Research Center *NASA Technical Memorandum* 112210
[6] Chan V S S, Heyes A L, Robinson D I and Turner J T 1995 Iodine absorption filters for Doppler global velocimetry *Meas. Sci. Technol.* **6** 784–94
[7] Seiler F and Oertel H 1985 Visualization of velocity fields with Doppler pictures *Flow Visualization III, Proc. 3rd Int., Symp. on Flow Visualization (Ann Arbor, MI)* pp 454–9
[8] Seiler F, George A, Leopold F, Srulijes J and Smeets G 1999 Flow velocities visualization using Doppler picture interference velocimetry *18th Int. Conf. on Instrumentation in Aerospace Simulation Facilities (Toulouse, France)* Paper 11.1–8
[9] Seiler F, Havermann M, George A, Leopold F and Srulijes J 2003 Planar velocity visualization in high-speed wedge flow using Doppler picture velocimetry (DPV) compared with particle image velocimetry (PIV) *J. Vis.* **6** 253–62
[10] Wernert P, Martinez B, George A, Leopold F and Seiler F 2005 Development of Doppler based planar velocimetry techniques for high-speed flows at ISL *8th Int. Symp. on Fluid Control, Measurement and Visualization (FLUCOME) (Chengdu, China)* Paper 316.1–18
[11] Nikiforov S B, Pavlov A A and Fomichov V P 2000 The use of field interferometers for panoramic LDA *9th Int. Symp. on Flow Visualization, Heriot-Watt University (Edinburgh)* Paper 226(1–6)
[12] Lu Z H, Charrett T O H, Ford H D and Tatam R P 2007 Mach–Zehnder interferometric filter based planar Doppler velocimetry (MZI-PDV) *J. Opt. A: Pure Appl. Opt.* **9** 1002–13
[13] Roehle I, Schodl R, Voigt P and Willert C 2000 Recent developments and applications of quantitative laser light sheet measuring techniques in turbomachinery components *Meas. Sci. Technol.* **11** 1023–35
[14] Meyers J F 1995 Development of Doppler global velocimetry as a flow diagnostics tool *Meas. Sci. Technol.* **6** 769–83
[15] McKenzie R L 1996 Measurement capabilities of planar Doppler velocimetry using pulsed lasers *Appl. Opt.* **35** 948–64
[16] Willert C, Stockhausen G, Beversdorff M, Klinner J, Lempereur C, Barricau P, Quest J and Jansen U 2005 Application of Doppler global velocimetry in cryogenic wind tunnels *Exp. Fluids* **39** 420–30
[17] Meyers J F, Lee J W, Fletcher M T, Cavone A A and Viramontes J A G 2006 Supersonic flow field investigation using a fiber-optic based Doppler global velocimeter *13th Int. Symp. on Applications of Laser Techniques to Fluid Mechanics (Lisbon, Portugal)* Paper 1019
[18] Schott A G http://www.schott.com (accessed 2008)
[19] Charrett T O H, Nobes D S and Tatam R P 2007 Investigation into the selection of viewing configurations for three component planar Doppler velocimetry (PDV) measurements *Appl. Opt.* **46** 4102–16
[20] Charrett T O H, Ford H D, Nobes D S and Tatam R P 2004 Two-frequency planar Doppler velocimetry (2ν-PDV) *Rev. Sci. Instrum.* **75** 4487–96
[21] Charrett T O H and Tatam R P 2006 Single-camera three component planar velocity measurements using two-frequency planar Doppler velocimetry (2ν-PDV) *Meas. Sci. Technol.* **17** 1194–206
[22] Nobes D S, Wieneke B and Tatam R P 2004 Determination of view vectors from image warping mapping functions *Opt. Eng.* **43** 407–14
[23] Takeda M, Ina H and Kobayashi S 1982 Fourier-transform method of fringe-pattern analysis for computer-based topography and interferometry *J. Opt. Soc. Am.* **72** 156–9
[24] Rajaratnam N 1976 *Turbulent Jets* (Amsterdam: Elsevier)